RESEARCH PAPER

Electrochemical Properties of $BaSr_{1-x}Gd_xCo_2O_{5+\delta}$ and $Ba_{0.5}Sr_{0.5-x}Gd_xCoO_{3-\delta}$ as a Cathode for Intermediate-Temperature Solid Oxide Fuel Cells

Sara Tafaroji*, Mansoor Farbod

* *sara.tafaroji@gmail.com*

Physics Department, Faculty of Science, Shahid Chamran University of Ahvaz, Ahvaz, I.R. Iran

Received: December 2025 **Revised: May 2026** **Accepted: July 2026**
DOI: 10.22068/ijmse.4528

Abstract: *The structural and electrochemical properties of Gd-doped perovskite oxides were investigated to improve the performance of solid oxide fuel cell (SOFC) cathodes. $Ba_{0.5}Sr_{0.5-x}Gd_xCoO_{3-\delta}$ and $BaSr_{1-x}Gd_xCo_2O_{5+\delta}$ (BSGC) compounds were synthesized via a sol–gel thermolysis method to elucidate the effects of Gd incorporation on crystal structure, microstructure, and electrochemical activity. X-ray diffraction (XRD) and scanning electron microscopy (SEM) confirmed the coexistence of simple and double perovskite phases, with Gd substitution leading to finer grains (down to 0.4 ± 0.14 μm) and improved phase homogeneity. Area-specific resistance (ASR) and conductivity measurements revealed a strong structure–performance relationship. The optimal composition, $Ba_{0.5}Sr_{0.3}Gd_{0.2}CoO_{3-\delta}$, exhibited an exceptionally low ASR of 0.12 Ω cm² at 700°C, which further decreased to a minimum of 0.04 Ω cm² at 850°C, significantly outperforming $GdBaCo_2O_{5+\delta}$ (GBCO) (1.76 Ω cm²). These findings demonstrate that rational structural design through rare-earth doping effectively enhances oxygen transport and electrochemical activity, providing a promising pathway for high-performance intermediate-temperature SOFC cathodes.*

Keywords: *$Ba_{0.5}Sr_{0.5-x}Gd_xCoO_{3-\delta}$, $BaSr_{1-x}Gd_xCo_2O_{5+\delta}$, Electrical conductivity, Electrochemical properties, Fuel cells.*

1. INTRODUCTION

Solid oxide fuel cells (SOFCs) are promising energy conversion devices that can efficiently generate electricity from a wide range of fuels with low emissions. However, one of the major challenges limiting their widespread commercialization is the poor cathode activity at reduced operating temperatures, which negatively impacts overall cell performance and efficiency. Furthermore, the high operational temperatures (typically above 800°C) required for conventional SOFCs cause severe interfacial reactions among cell components, leading to degradation and reduced long-term stability [1]. To address these issues, extensive research has focused on developing cathode materials that exhibit high catalytic activity, excellent electronic conductivity, efficient surface oxygen exchange, and rapid oxygen ion diffusion at intermediate to low temperatures (500–750°C). These efforts have resulted in the discovery of numerous mixed ionic and electronic conducting (MIEC) oxides with diverse crystal structures. Among them, perovskite-type oxides ($(AA')(BB')O_{3-\delta}$) such as $La_{0.6}Sr_{0.4}Co_{0.2}Fe_{0.8}O_{3-\delta}$ (LSCF) and $Ba_{0.5}Sr_{0.5}Co_{0.8}Fe_{0.2}O_{3-\delta}$ (BSCF) [2, 3] have attracted significant attention due to their high oxygen diffusion coefficients and excellent surface catalytic properties. Other perovskite-related structures, including Ruddlesden–Popper structures ($A_{n+1}B_nO_{3n+1}$) such as $La_2NiO_{4+\delta}$, $(Nd_{0.9}La_{0.1})_2Ni_{0.75}Cu_{0.25}O_4$ (NLNC) [4], and double perovskite oxides ($AA'B_2O_{5+\delta}$) such as $BaGdCo_2O_{5+\delta}$ (BGC) and $SmBaCo_2O_{5+\delta}$ (SBCO) [5, 6], have also demonstrated promising electrochemical performance.

Recently, layered double perovskite compounds have emerged as attractive candidates for intermediate- and low-temperature SOFC cathodes. These materials feature alternating layers of alkaline-earth and rare-earth cations at the A-site, forming a distinctive structural arrangement along the *c*-axis. The B-site is typically occupied by transition metal ions such as Co or Mn in ($AA'B_2O_{5+\delta}$) compounds, or by alternating transition metals in ($A_2BB'O_{5+\delta}$) structures [6, 7]. This unique layered configuration enhances oxygen diffusion and electronic conductivity, resulting in improved oxygen reduction reaction (ORR) kinetics and overall fuel cell performance [8-11].

Among various candidates, cobaltite-based perovskite oxides have attracted significant attention due to their exceptional mixed ionic-electronic conductivity and rapid oxygen reduction reaction (ORR) kinetics at intermediate temperatures [12]. To further enhance the performance of these materials, researchers have explored various A-site and B-site doping strategies. For instance, partial substitution of Co with Ca has been reported to increase the electronic density of states and catalytic activity

[13]. Substitution with other transition metals can reduce thermal expansion and improve catalytic stability [9, 14, 15]. In $GdBaCo_2O_{5+\delta}$, lanthanide substitution at the A-site has been shown to expand the triple-phase boundary (TPB) between the electrolyte, electrode, and gas phase, thereby enhancing ORR activity [16, 17]. Similarly, increasing Sr content in place of Ba at the A-site improves both electrical conductivity and oxygen ion transport [18-20].

Various synthesis routes—such as floating-zone melting, EDTA–citrate complexation, and solid-state reactions—have been employed to prepare double perovskite oxides, with processing parameters (especially calcination temperature) found to have a significant influence on microstructure and oxygen reduction activity [7, 21-23].

In this study, $BaSr_{1-x}Gd_xCo_2O_{5+\delta}$ and $Ba_{0.5}Sr_{0.5-x}Gd_xCoO_{3-\delta}$ (BSGC) powders were synthesized via the sol–gel thermolysis method to explore the effects of Gd doping on structure and electrochemical performance. The investigation focused on phase formation, particle size evolution, electrical conductivity, and impedance behavior over a range of temperatures. A symmetric cell configuration employing samaria-doped ceria (SDC) as the electrolyte and BSGC as the cathode was used for impedance analysis. This work aims to elucidate the relationship between structural design and electrochemical performance, thereby contributing to the development of efficient cathode materials for intermediate-temperature SOFCs.

2. EXPERIMENTAL PROCEDURES

2.1. Synthesis of $BaSr_{1-x}Gd_xCo_2O_{5+\delta}$ (BSGC)

BSGC powders were synthesized via a sol–gel thermolysis method, chosen for its simplicity and ability to produce homogeneous fine powders. Urea was used as the primary fuel, while polyvinyl alcohol (PVA) served both as a dispersing agent and as a secondary fuel.

Stoichiometric amounts of $Ba(NO_3)_2$, $Sr(NO_3)_2$, $Co(NO_3)_3.6H_2O$, and $Gd(NO_3)_3.6H_2O$ were dissolved in deionized water to form the precursor solution. The molar ratio of fuel to nitrates was maintained at 8.5, which was also applied to the PVA-to-nitrate ratio. Separately, aqueous solutions of PVA and urea were prepared. The nitrate solution was gradually added to the PVA solution under continuous stirring, followed by the addition of the urea solution.

The resulting mixture was heated to 100°C with constant stirring until a viscous sol was obtained. After approximately 3 hours at 120°C, the sol transformed into a gel. The gel was then pre-calcined at 650°C for 5 h to remove organic residues, followed by calcination at 1000°C for 5 h to obtain single-phase BSGC powders.

2.2. Synthesis of Samaria-Doped Ceria

Samaria-doped ceria (SDC) with the nominal composition $Sm_{0.2}Ce_{0.8}O_{1.9}$ was synthesized via the solid-state reaction method, following procedures reported in previous studies [3]. The resulting SDC was used as the electrolyte material for symmetric cell fabrication.

2.3. Preparation of Cells and Bars

For electrical conductivity measurements, the synthesized BSGC powders were uniaxially pressed into bar-shaped pellets under a pressure of 100 MPa and sintered at 1150°C for 5 h. The heating rate was carefully controlled at $5°C\cdot min^{-1}$ to ensure uniform densification.

For electrochemical impedance spectroscopy (EIS) analysis, symmetric cells were fabricated using SDC as the electrolyte and BSGC as the cathode material. The SDC electrolyte pellets were prepared by pressing the SDC powder at 100 MPa and sintering at 1500°C for 5 h, yielding a dense structure suitable for impedance measurements.

A BSGC slurry was prepared by mixing the synthesized powder with ethyl cellulose in a 60:40 (wt%) ratio, followed by the addition of α-terpineol to adjust viscosity and maintain a solid content of approximately 5 wt%. The mixture was thoroughly ground in an agate mortar for 30 min to ensure homogeneity [24]. The resulting slurry was brush-coated onto both sides of the SDC electrolyte pellet and dried at 70°C. The coating process was repeated three times to achieve uniform cathode layers. The assembled cells were then annealed at 1100°C for 2 h in air. Finally, silver paste was applied on both sides of the cathode layers to serve as current collectors.

2.4. Characterization of Samples

The crystal structure and phase purity of the synthesized powders were analyzed using X-ray diffraction (XRD) (Philips PW-1840 diffractometer) with Cu Kα radiation (λ= 1.5418 Å), scanned over the 2θ range of 10–90° at room temperature.

The morphology and particle size of the powders were examined using scanning electron microscopy (SEM) (LEO 1455 VP). Electrical conductivity

measurements were performed using the standard four-probe method in air over the temperature range of 300–850°C.

For AC impedance spectroscopy, symmetric cells with BSGC and BSGC+SDC cathodes were tested using a Solartron Analytical 1260 Impedance/ Gain-Phase Analyzer coupled with a Solartron Analytical 1287 Potentiostat/Galvanostat.

Measurements were conducted in air over a frequency range of 1 Hz–1 MHz, with an applied AC amplitude of 20 mV. The experiments were carried out in a tube furnace under temperatures ranging from 600 to 850°C to evaluate the impedance and electrochemical behavior of the samples.

3. RESULTS AND DISCUSSION

Fig. 1 presents the X-ray diffraction (XRD) patterns of $BaSr_{1-x}Gd_xCo_2O_{5+\delta}$ and $Ba_{0.5}Sr_{0.5-x}Gd_xCoO_{3-\delta}$ (BSGC) powders, illustrating the effect of Gd substitution on their crystal structures. The diffraction data were analyzed using HighScore Expert software and compared with standard JCPDS reference cards. The $Ba_{0.5}Sr_{0.5}CoO_{3-\delta}$ sample exhibits a single-phase hexagonal perovskite structure with a space group of $P6_3/mmc$, confirming high phase purity and the absence of detectable secondary phases. These results are consistent with those reported previously [25, 26]. For samples with x< 0.2, the hexagonal perovskite phase remains dominant. However, progressive incorporation of Gd leads to systematic changes in the diffraction patterns, suggesting a structural transition toward a double perovskite phase with tetragonal P4/ symmetry. This transformation is associated with the two-dimensional ordering of oxygen vacancies along the (0 0 1) planes. In contrast, the diffraction pattern of $BaGdCo_2O_{5+\delta}$ matches reference code 96-140-2617 and agrees well with previously published data [22, 23, 27, 28]. At intermediate compositions (x= 0.3 and x= 0.4), the coexistence of hexagonal and tetragonal reflections indicates the presence of a mixed-phase region, characteristic of the transition between the simple and double perovskite structures. Similar behavior has been reported in related systems [29, 30]. The structural evolution can be attributed to the ionic size mismatch among Ba^{2+} (1.38 Å), Sr^{2+} (1.21 Å), and Gd^{3+} (1.12 Å). The substitution of Sr^{2+} with the smaller Gd^{3+} ion induces lattice distortions and promotes the formation of alternating Gd–O and Ba–O layers along the *c*-axis. In the double perovskite structure, oxygen vacancies preferentially occupy the Gd–O layers, a phenomenon that becomes more pronounced with increasing Gd concentration [31-33].

Bars and pellets prepared for electrical conductivity measurements were sintered at 1150°C for 5 h. To verify the structural stability after sintering, the XRD pattern of the $BaGdCoO_{5+\delta}$ bar was recorded at room temperature over the 2θ range of 10°–90°, as shown in Fig. 2. The results confirm that no phase transformation occurred during the sintering process.

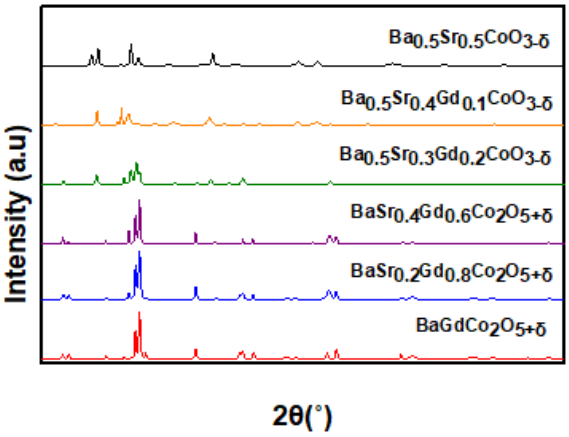

Fig. 1. XRD patterns of $BaSr_{1-x}Gd_xCo_2O_{5+\delta}$ and $Ba_{0.5}Sr_{0.5-x}Gd_xCoO_{3-\delta}$ (BSGC) powders with different amounts of x values

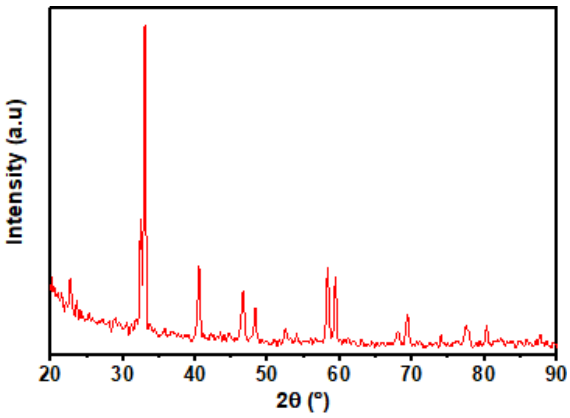

Fig. 2. XRD patterns of $BaGdCo_2O_{5+\delta}$ bar after sintering at 1150°C for 5 h

To further elucidate the phase evolution and investigate the structural changes as a function of Gd doping, a detailed comparative XRD analysis was performed. Figure 3 displays the XRD patterns of the end-member compositions, pure hexagonal $Ba_{0.5}Sr_{0.5}CoO_{3-\delta}$ and pure tetragonal $BaGdCo_2O_{5+\delta}$, alongside the intermediate $Ba_{0.5}Sr_{0.3}Gd_{0.2}CoO_{3-\delta}$ sample.

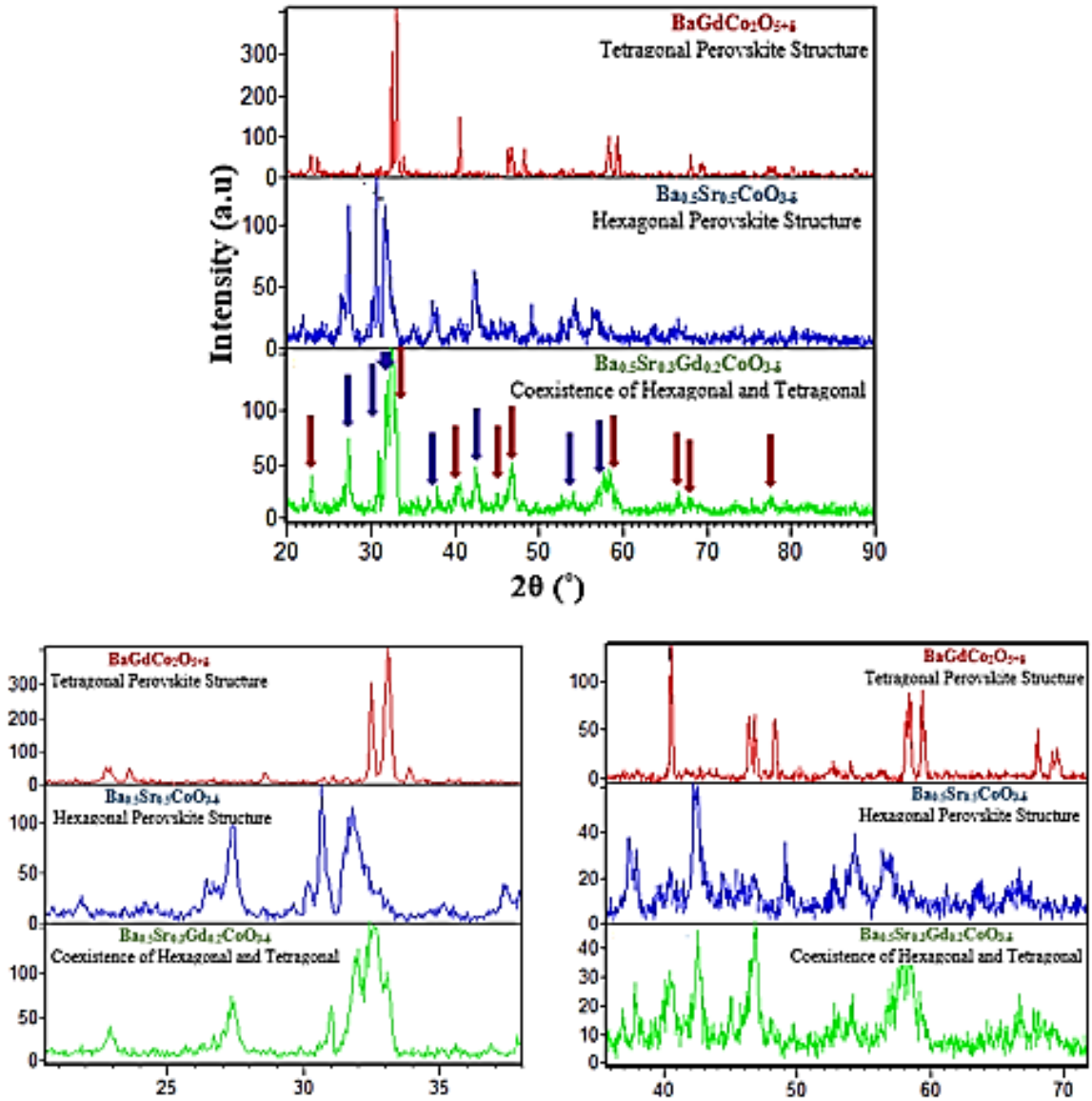

Fig. 3. XRD patterns of $BaGdCo_2O_{5+\delta}$, $Ba_{0.5}Sr_{0.3}Gd_{0.2}CoO_{3-\delta}$ and $Ba_{0.5}Sr_{0.5}CoO_{3-\delta}$ (BSGC) powders

As marked by the color-coded arrows in Figure 3, the intermediate composition (x= 0.2) exhibits a clear superposition of Bragg reflections belonging to both symmetries. The blue arrows index the characteristic peaks of the hexagonal perovskite structure, while the red arrows correspond to the reflections of the tetragonal perovskite phase. To eliminate any phase ambiguity and provide a closer inspection, high-resolution magnified views of the critical 2θ regions (20°–38° and 36°–72°) are presented in the lower panels of Figure 3. In these magnified profiles, the simultaneous survival of distinct reflection peaks and notable peak splitting within the intermediate sample can be clearly observed. This visible coexistence of diffraction lines from both the hexagonal and tetragonal systems provides strong qualitative evidence of a two-phase coexistence region at this specific dopant concentration, rather than a single-phase transformation.

Scanning electron microscopy (SEM) images of the synthesized powders are shown in Fig. 4. All samples exhibit a porous morphology typical of materials prepared by the sol–gel combustion route. The observed porosity originates from the release of gaseous by-products during the combustion of organic precursors and the subsequent removal of residual carbonaceous species during sintering. This open-pore structure is advantageous for applications involving oxygen transport or electro-chemical activity, as it facilitates gas diffusion and increases the effective surface area.

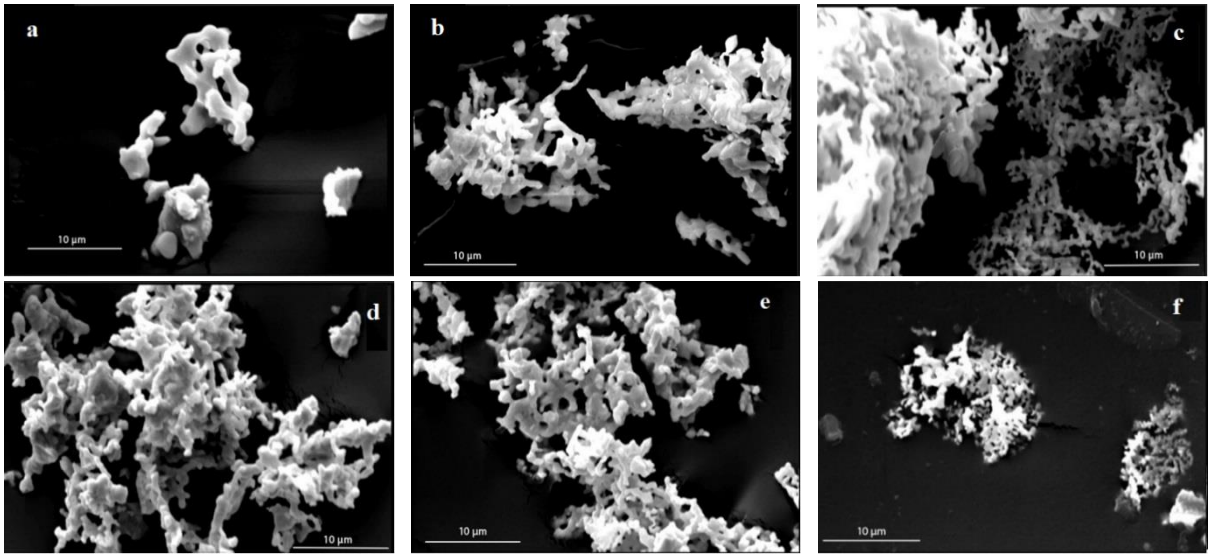

Fig. 4. A scanning electron micrograph image of a) $Ba_{0.5}Sr_{0.5}CoO_{3-\delta}$, b) $Ba_{0.5}Sr_{0.4}Gd_{0.1}CoO_{3-\delta}$, c) $Ba_{0.5}Sr_{0.3}Gd_{0.2}CoO_{3-\delta}$, d) $BaSr_{0.4}Gd_{0.6}CoO_{5+\delta}$, e) $BaSr_{0.2}Gd_{0.8}CoO_{5+\delta}$, f) $BaGdCoO_{5+\delta}$

Despite the overall morphological similarity, notable variations in particle size were observed as a function of Gd and Sr content. The undoped $Ba_{0.5}Sr_{0.5}CoO_{3-\delta}$ sample exhibits the largest grains, indicative of extensive grain coarsening during sintering. In contrast, the $BaGdCo_2O_{5+\delta}$ sample (x= 1.0), which contains no Sr, shows the smallest and most uniformly distributed grains. This suggests that the incorporation of Gd^{3+} ions, which possess a smaller ionic radius than Sr^{2+}, inhibits grain growth by introducing local lattice distortions and increasing diffusion barriers during sintering.

For the intermediate compositions $Ba_{0.5}Sr_{0.4}Gd_{0.1}CoO_{3-\delta}$, $Ba_{0.5}Sr_{0.3}Gd_{0.2}CoO_{3-\delta}$, $BaSr_{0.4}Gd_{0.6}Co_2O_{5+\delta}$, and $BaSr_{0.2}Gd_{0.8}Co_2O_{5+\delta}$, the particle sizes are relatively uniform, ranging from 0.6 to 0.7 µm. This trend suggests that a balanced Sr/Gd ratio promotes moderate grain growth, leading to a homogeneously distributed microstructure. Such microstructural uniformity is beneficial for improving both mechanical integrity and electrochemical stability. The estimated average pore diameters fall within the 0.2–0.4 µm range, consistent with porosity values typically reported for sol–gel-derived perovskite oxides [35, 36]. The interconnected pore network and submicrometer particle sizes are expected to enhance oxygen ion mobility and reduce polarization losses in electrochemical applications.

Overall, these results indicate that partial substitution of Sr by Gd effectively refines the grain size and stabilizes the porous framework without significantly altering the morphology. The relationship between these microstructural features and the electrical conductivity of the samples will be discussed below.

Fig. 5 presents the particle size distribution histograms for the various samples, together with their corresponding log-normal fitted curves, mean particle sizes, and standard deviations. Particle size measurements were obtained using the Digimizer software in conjunction with scanning electron microscopy (SEM) images. Analysis of these images and the associated histograms in Fig. 5 reveals a clear trend: increasing substitution of gadolinium (Gd) for strontium (Sr) results in a reduction in particle size. This decrease can be primarily attributed to two key factors. The first is the initial incorporation of Gd (x= 0.1) into the $Ba_{0.5}Sr_{0.5-x}Gd_xCoO_{3-\delta}$ compound, which causes the average particle size to decrease from 1.67 µm to 0.97 µm. The second factor is associated with the complete replacement of Sr (x= 1) in the $BaSr_{1-x}Gd_xCo_2O_{5+\delta}$ composition, leading to a further reduction in average particle size from 0.6 µm to 0.4 µm. For intermediate compositions, the particle sizes remain relatively stable. These observations indicate that both the morphology and intrinsic properties of materials used as solid oxide fuel cell (SOFC) cathodes play a crucial role in determining their oxygen reduction reaction (ORR) performance. In general, cathodes with smaller particle sizes and higher porosity exhibit enhanced ORR activity [3, 34, 35].

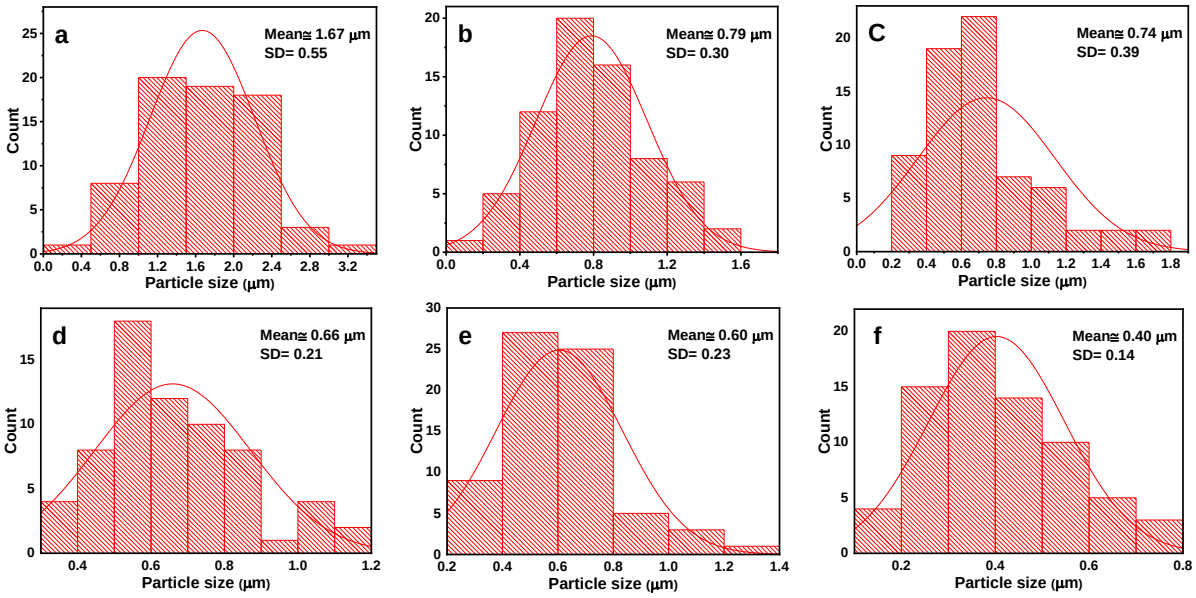

Fig. 5. The size distribution of average particle size and a standard deviation (SD) of a) $Ba_{0.5}Sr_{0.5}CoO_{3-\delta}$, b) $Ba_{0.5}Sr_{0.4}Gd_{0.1}CoO_{3-\delta}$, c) $Ba_{0.5}Sr_{0.3}Gd_{0.2}CoO_{3-\delta}$, d) $BaSr_{0.4}Gd_{0.6}Co_2O_{5+\delta}$, e) $BaSr_{0.2}Gd_{0.8}Co_2O_{5+\delta}$, f) $BaGdCo_2O_{5+\delta}$

Fig. 6 presents scanning electron microscopy (SEM) images of the $BaGdCo_2O_{5+\delta}$ pellet cross-section, illustrating the uniformity of the cathode layer and its strong adhesion to the electrolyte. The cathode layer thickness for these samples was measured using Digimizer software, with all values falling within the range of 20 to 30 micrometers. The SEM images further confirm that the sample exhibits high density after sintering. Low electrolyte density, characterized by the presence of holes or cracks, can result in gas leakage, thereby reducing the efficiency of the cell and contributing to fuel loss. Fig. 7 illustrates the total direct current (DC) conductivity of various synthesized powders, measured using the standard four-probe technique in air over a temperature range of 250°C to 850°C. To ensure the reliability and reproducibility of the electrical measurements, the conductivity data for all samples are presented with their respective standard deviations (error bars), as shown in Fig. 7. The inset in Fig. 7 provides a magnified view with clear error bars for the lower conductivity ranges. As previously discussed, these mixed ionic and electronic conduction (MIEC) materials, owing to their hole conduction and oxygen vacancies, exhibit both ionic and electronic conductivities, contributing to their exceptional conductive properties [36]. For the four samples with x >0.1 ($BaSr_{1-x}Gd_xCo_2O_{5+\delta}$), a similar trend is observed: conductivity increases at lower temperatures and then decreases at higher temperatures, demonstrating semiconducting behavior. The highest conductivity, approximately 520.57 $S\cdot cm^{-1}$ at 350°C, was recorded for the $BaGdCo_2O_{5+\delta}$ sample. This value is roughly twenty times greater than the maximum conductivity of BSC at 850°C, after which conductivity gradually decreases with increasing temperature, as observed for the other three samples (c, d, and e).

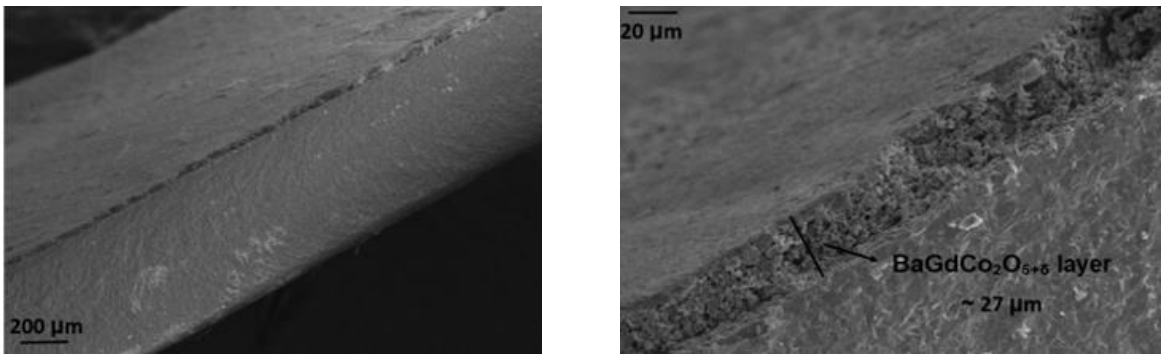

Fig. 6. Scanning electron micrograph images of $BaGdCo_2O_{5+\delta}$ pellet cross section

This suggests that the structural properties and the presence of oxygen vacancies play a more significant role in conductivity than the small particle size alone, as increased grain boundaries can reduce electron conductivity. For these four samples, the transition from semiconducting to metallic behavior is evident [37], which can be attributed to charge neutrality and variations in the valence states of Co cations due to oxygen vacancies. This remarkably high electronic transport in the low-to-intermediate temperature range is characteristic of a thermally activated small polaron hopping mechanism. The doping of Gd within the Ba–Sr cobaltite framework facilitates a mixed-valence state of cobalt ions (Co^{3+}/Co^{4+}). The overlap between the cobalt 3d orbitals and oxygen 2p orbitals enhances the electron-hole carrier concentration, promoting rapid charge transfer along the Co–O–Co pathways. Similar high-magnitude electronic conductivities have been established for related cobaltite perovskites, validating the structural optimization achieved in this work [38].

In both the double perovskite and perovskite structures, maintaining the average oxidation state of Co ions helps preserve the electrical neutrality of the crystal. In the double perovskite structure, this oxidation state ranges from +2.5 (δ= 0) to +3.5 (δ= 1), while in the perovskite structure, it ranges from +4 (δ= 0) to +2 (δ= 1). In the double perovskite structure, various superstructures can form, such as 1ap × 2ap × 2ap and 3ap × 3ap × 2ap (relative to the subcell), or 1ap × 1ap × 2ap, depending on the space group and magnetic cell arrangement, where "ap" refers to the unit cell parameter for the perovskite-type cubic structure. In the case of $BaGdCo_2O_{5+\delta}$ with a 1ap × 2ap × 2ap superstructure, Co ions are coordinated with five or six oxygen ions, depending on the arrangement of oxygen vacancies in the [GdO_δ] layer. This coordination allows Co ions to adopt oxidation states of +2, +3, or +4, contributing to the material's excellent properties [11, 21].

The observed decrease in conductivity at higher temperatures can be attributed to the formation of a significant number of oxygen vacancies. The reduction of Co^{4+} to Co^{3+} leads to the creation of these vacancies, which in turn reduces the concentration of hole charge carriers, decreases Co–O covalence, and ultimately lowers the electrical conductivity at elevated temperatures. Furthermore, the presence of oxygen vacancies disrupts the O–Co–O periodic potential, resulting in carrier localization [39, 40].

At temperatures below 350°C, holes act as the majority charge carriers in cobalt-based perovskites. Within this temperature range, the Co ions exist in both trivalent (Co^{3+}) and tetravalent (Co^{4+}) states, which promotes a polaron hopping conduction mechanism. This behavior is attributed to the increased oxygen concentration in the material, which enhances the overlap of B-O-B bonds between the B-site lattice cations and oxygen. The reduction in the B-O bond distance facilitates electron hopping, thereby improving the efficiency of charge conduction. As a result, electrical conductivity increases with temperature, until oxygen loss occurs upon further heating, typically observed at temperatures above 300°C [20, 36, 41, 42].

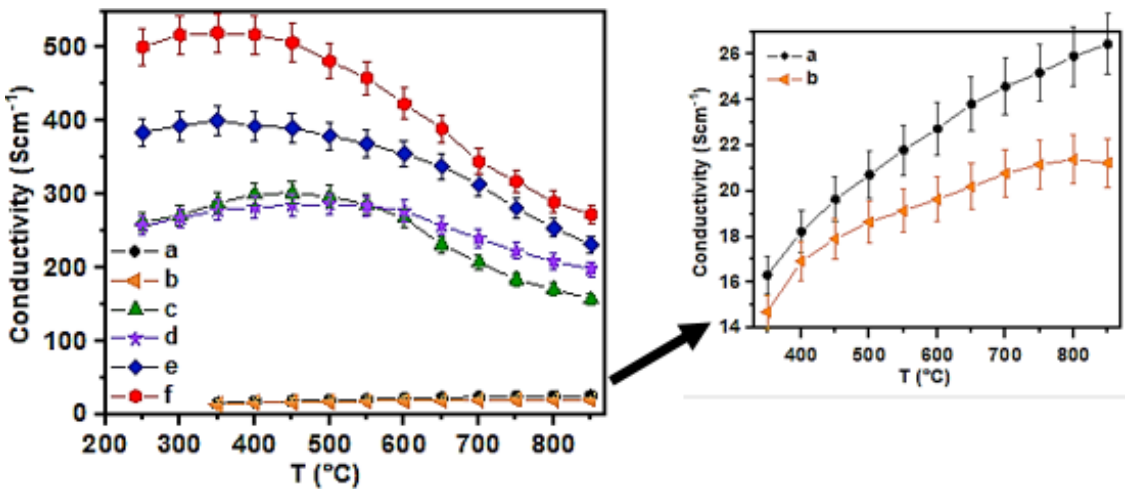

Fig. 7. Total conductivity of a) $Ba_{0.5}Sr_{0.5}CoO_{3-\delta}$, b) $Ba_{0.5}Sr_{0.4}Gd_{0.1}CoO_{3-\delta}$, c) $Ba_{0.5}Sr_{0.3}Gd_{0.2}CoO_{3-\delta}$, d) $BaSr_{0.4}Gd_{0.6}Co_2O_{5+\delta}$, e) $BaSr_{0.2}Gd_{0.8}Co_2O_{5+\delta}$, f) $BaGdCo_2O_{5+\delta}$. The error bars represent the standard deviations of the measurements, and the inset shows a magnified view for low-conductivity samples

For both BSC and $Ba_{0.5}Sr_{0.4}Gd_{0.1}CoO_{3-\delta}$, conductivity continues to increase with temperature across the entire studied range, which suggests metallic behavior. However, BSC demonstrates a higher electrical conductivity of 26 $S \cdot cm^{-1}$ at 850°C compared to $Ba_{0.5}Sr_{0.4}Gd_{0.1}CoO_{3-\delta}$. The reduced conductivity observed in $Ba_{0.5}Sr_{0.4}Gd_{0.1}CoO_{3-\delta}$ can be attributed to a decrease in orbital overlap resulting from the smaller ionic radius of Gd^{3+}, which leads to an increased bending of the O-Co-O bond in the crystal structure [39, 43]. As the Gd concentration increases, the conduction mechanism changes due to structural modifications in the material. The conducting behavior of perovskite materials that incorporate both oxygen ions and electrons is heavily influenced by the crystal structure and the concentration of oxygen vacancies [44]. This phenomenon is exemplified by the contrasting conductivity behavior observed in the samples $Ba_{0.5}Sr_{0.3}Gd_{0.2}CoO_{3-\delta}$ (c) and $BaSr_{0.4}Gd_{0.6}Co_2O_{5+\delta}$ (d), where their conductivity curves intersect around 550°C. The overall trend in conductivity is as follows: BGC >$BaSr_{0.2}Gd_{0.8}Co_2O_{5+\delta}$ >… >BSC >$Ba_{0.5}Sr_{0.4}Gd_{0.1}CoO_{3-\delta}$, indicating that doping the A-site with Gd enhances the electrical conductivity of BSC.

According to the Arrhenius equation, the conduction mechanism in materials exhibiting small adiabatic polaron hopping has been calculated from the following relation [36, 45]:

$$\sigma = \frac{A}{T}\exp\left(\frac{-E_a}{k_B T}\right) \quad (1)$$

where σ(T) is the electrical conductivity at temperature T, A is the pre-exponential factor, E_a is the activation energy, k_B is the Boltzmann constant, and T is the absolute temperature.

The activation energy values, derived from the slopes of the conductivity versus inverse temperature plots shown in Fig. 8, are summarized in Table 1. Notably, the samples BSC and $Ba_{0.5}Sr_{0.4}Gd_{0.1}CoO_{3-\delta}$ exhibit a consistent activation energy across the entire measured temperature range. In contrast, other samples show two distinct activation energy values, corresponding to different temperature ranges. An analysis of the activation energy E_a reveals a clear trend: as the Gd content increases, the perovskite's oxygen reduction reaction (ORR) activity improves. This is particularly evident in the $BaSr_{0.4}Gd_{0.6}Co_2O_{5+\delta}$ sample, where structural modifications due to the larger Gd cations promote the formation of more oxygen vacancies. The higher oxygen vacancy concentration leads to an enhanced distribution of negative charges across neighboring Co ions, which in turn increases the electron density and facilitates the ORR activity [42]. While the activation energy values for most samples are relatively small and closely aligned, there are some notable variations. The highest activation energy, 0.13 eV, is observed in $Ba_{0.5}Sr_{0.5}CoO_{3-\delta}$, while the lowest, 0.03 eV, is found in $BaSr_{0.4}Gd_{0.6}Co_2O_{5+\delta}$ at temperatures exceeding 600°C.

This suggests that the Gd doping significantly influences the conduction behavior, especially at elevated temperatures, likely due to enhanced ionic conductivity driven by the increased oxygen vacancy concentration and the resulting electronic effects. The performance of $BaSr_{1-x}Gd_xCo_2O_{5+\delta}$ and $Ba_{0.5}Sr_{0.5-x}Gd_xCoO_{3-\delta}$ samples was evaluated in an electrochemical system across a range of temperatures (550–850°C, with 50°C increments).

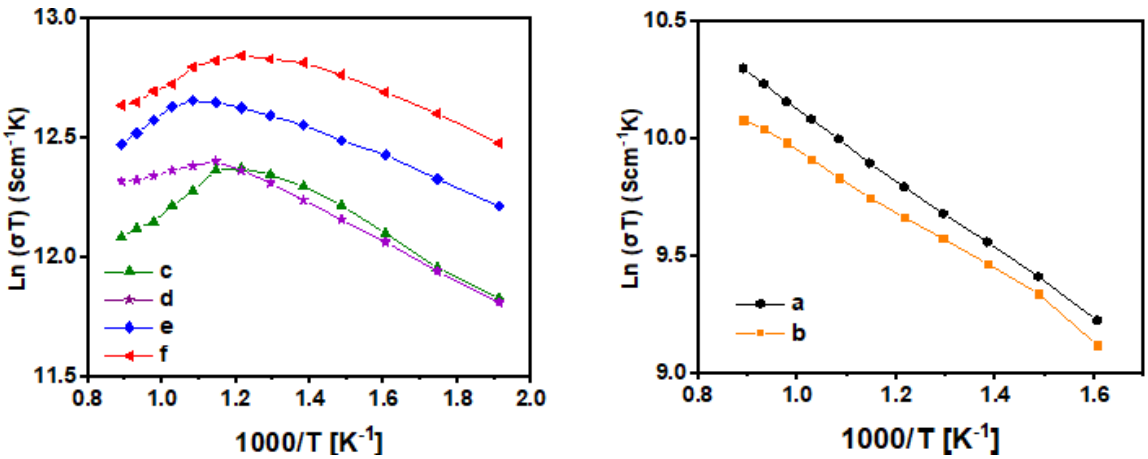

Fig. 8. The Arrhenius plots of conductivities of all measured a) $Ba_{0.5}Sr_{0.5}CoO_{3-\delta}$, b) $Ba_{0.5}Sr_{0.4}Gd_{0.1}CoO_{3-\delta}$, c) $Ba_{0.5}Sr_{0.3}Gd_{0.2}CoO_{3-\delta}$, d) $BaSr_{0.4}Gd_{0.6}Co_2O_{5+\delta}$, e) $BaSr_{0.2}Gd_{0.8}Co_2O_{5+\delta}$, f) $BaGdCo_2O_{5+\delta}$ samples versus 1000 T^{-1} (K^{-1})

Table 1. Activation energies of the BSGC samples were calculated using the Arrhenius equation

Sample	E_a (eV)					
	T< 550°C	T< 550°C	T< 600°C	T >600°C	T >650°C	T >650°C
$Ba_{0.5}Sr_{0.5}CoO_{3-\delta}$	0.13	0.13	0.13	0.13	0.13	0.13
$Ba_{0.5}Sr_{0.4}Gd_{0.1}CoO_{3-\delta}$	0.11	0.11	0.11	0.11	0.11	0.11
$Ba_{0.5}Sr_{0.3}Gd_{0.2}CoO_{3-\delta}$	0.07	0.09	0.09	0.09	0.09	0.09
$BaSr_{0.4}Gd_{0.6}Co_2O_{5+\delta}$	0.07	0.07	0.07	0.03	0.03	0.03
$BaSr_{0.2}Gd_{0.8}Co_2O_{5+\delta}$	0.05	0.05	0.05	0.05	0.05	0.08
$BaGdCo_2O_{5+\delta}$	0.05	0.06	0.06	0.06	0.06	0.06

This evaluation focused on the Area Specific Resistance (ASR) of symmetrical cells tested in air. Fig. 9 presents the impedance spectra of $BaSr_{0.2}Gd_{0.8}Co_2O_{5+\delta}$ cathodes on a Samaria-doped ceria (SDC) electrolyte, while the impedance spectra for the other synthesized samples are shown in Fig. 10.

The Area Specific Resistance (ASR) was determined by calculating the difference between the two intercepts of the arcs on the real axis of the Nyquist plot. The intercept at high frequency corresponds to the resistance of the electrolyte and lead wires, while the impedance data were analyzed using the circuit model R_s/R_1 (CPE_1)/R_2 (CPE_2), as shown in Fig. 9. In this model, Rs represents the ohmic resistance associated with the electrolyte and wires, while R_1 and R_2 correspond to the polarization resistances.

The electrode impedance is divided into two components: charge-related and non-charge-related, based on the arcs observed at high frequencies and in the medium-to-low frequency range. Specifically, the high-frequency arc (R_1) is associated with charge transfer processes, including the migration and diffusion of oxygen ions from the triple-phase boundary into the electrolyte lattice, as well as the overall electrochemical oxygen reduction reaction (ORR). Conversely, the low-frequency arc (R_2) reflects resistance originating from the absorption-desorption of oxygen at both the surface and bulk of the cathode, solid-state diffusion, and inner/outer gas-phase diffusion [46, 47].

Therefore, the total polarization resistance R_p of the cathodes is the sum of R_1 and R_2. As seen in Fig. 9, the high-frequency arc becomes larger with increasing temperature, while the low-frequency arc remains relatively smaller. At 850°C, the high-frequency arc for $BaSr_{0.2}Gd_{0.8}Co_2O_{5+\delta}$ significantly expands, indicating an increase in charge transfer at elevated temperatures.

Fig. 11 presents the impedance resistance values for different synthesized cathodes in symmetric cells at 700°C. Notably, in both perovskite and double perovskite structures, the polarization resistance (R_p) increases with the amount of Gd doping. However, a significant change in R_p is observed when altering the structure of the $Ba_{0.5}Sr_{0.3}Gd_{0.2}CoO_{3-\delta}$ sample. This behavior can be attributed to the strong Gd-O bonding interactions, which hinder the absorption and desorption of mobile oxygen species from the oxygen lattice.

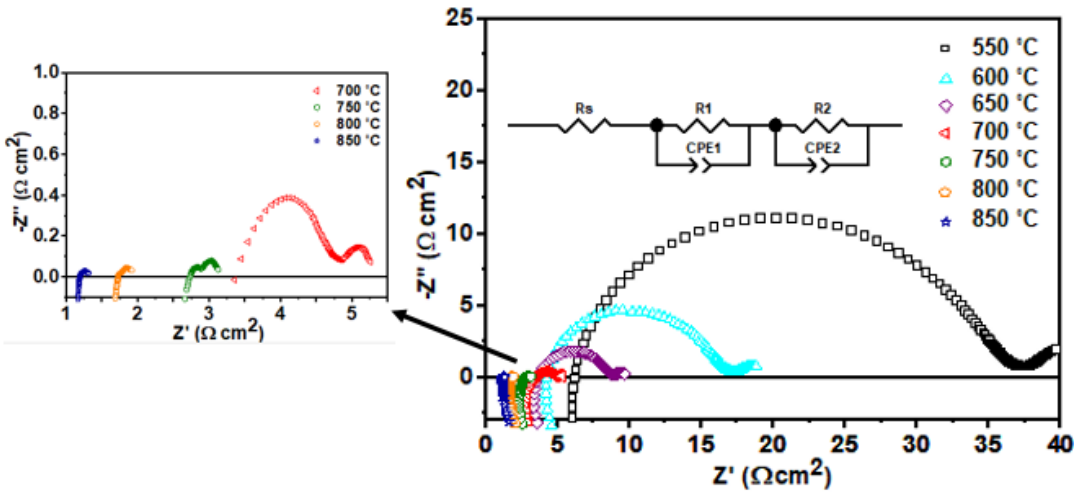

Fig. 9. The electrochemical impedance spectroscopy (EIS) of the symmetric cell with $BaSr_{0.2}Gd_{0.8}Co_2O_{5+\delta}$ cathode at different temperatures

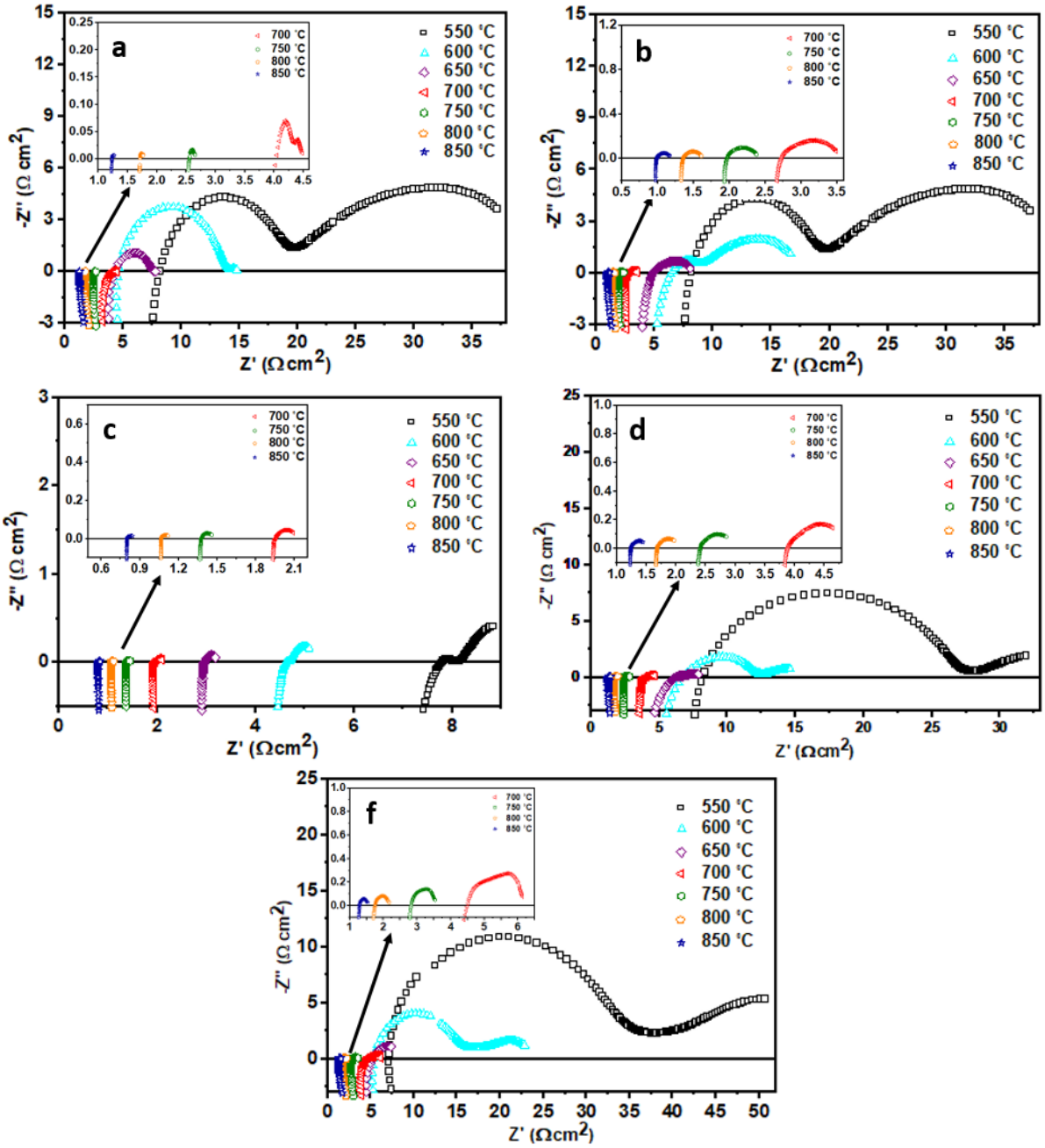

Fig. 10. The electrochemical impedance spectroscopy (EIS) of the symmetric cells with a) $Ba_{0.5}Sr_{0.5}CoO_{3-\delta}$, b) $Ba_{0.5}Sr_{0.4}Gd_{0.1}CoO_{3-\delta}$, c) $Ba_{0.5}Sr_{0.3}Gd_{0.2}CoO_{3-\delta}$, d) $BaSr_{0.4}Gd_{0.6}Co_2O_{5+\delta}$, f) $BaGdCo_2O_{5+\delta}$ cathode at different temperatures

As a result, the oxygen kinetics related to bulk diffusion and surface exchange, which rely on the mobility of oxygen species, can be negatively impacted by a high Gd concentration [48]. Interestingly, while the $BaGdCo_2O_{5+\delta}$ sample exhibits higher electrical conductivity than the other samples, it also demonstrates greater polarization resistance. This behavior is consistent with the explanation above, where the Gd-O bond strength interferes with the movement of oxygen species. As discussed in relation to Table 1, the activation energies (E_a) for all samples are quite similar, indicating comparable oxygen reduction reaction (ORR) activity across the materials. However, other factors influence the polarization resistance, such as surface reaction activity, interfacial resistance (i.e., effective pathways for the transfer of oxygen ions, intermediates, or electrons), electrode microstructure, and the decrease in electron- hole species with increasing oxygen vacancy concentration.

The Arrhenius plots of the ASRs derived from the

impedance results in Fig. 9 and Fig. 10 are shown in Fig. 11. The activation energies were calculated using the following equation:

$$\log R_p = \log R_0 - \frac{E_a}{2.303RT} \quad (2)$$

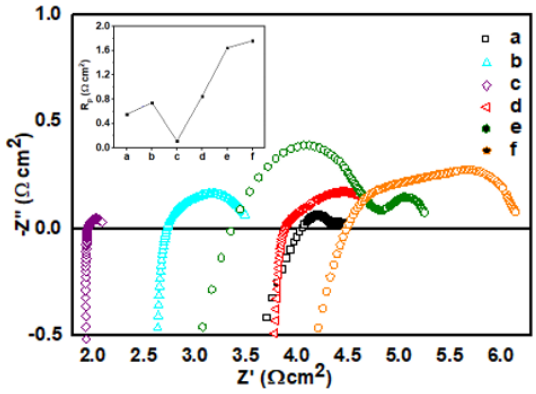

Fig. 11. The electrochemical impedance spectroscopy (EIS) of the symmetric cells with a) $Ba_{0.5}Sr_{0.5}CoO_{3-\delta}$, b) $Ba_{0.5}Sr_{0.4}Gd_{0.1}CoO_{3-\delta}$, c) $Ba_{0.5}Sr_{0.3}Gd_{0.2}CoO_{3-\delta}$, d) $BaSr_{0.4}Gd_{0.6}Co_2O_{5+\delta}$, e) $BaSr_{0.2}Gd_{0.8}Co_2O_{5+\delta}$, f) $BaGdCo_2O_{5+\delta}$ cathodes at 700°C

Where R is the universal gas constant, T is the absolute temperature, and R_0 refers to the pre-exponential factor in Equation 2. The activation energy (E_a) reflects all cathode processes, including oxygen adsorption, dissociation, bulk and surface diffusion, as well as self-diffusion through the electrolyte [49, 50]. The E_a values for all synthesized samples, considering both high and low-frequency polarization resistance and total polarization resistance, are summarized in Table 2, based on the slopes of the graphs in Fig. 12. A noticeable change in the slope of the Arrhenius plot for the samples, compared to a cell with a BSC cathode, is evident in Fig. 12. The changes for samples (c) and (d) are particularly pronounced. This variation can be attributed to differences in the mechanism of the oxygen reduction reaction [51]. The error bars for the Log ASR data in the Arrhenius plots (Fig. 12) were determined by propagating the fitting uncertainties of the polarization resistance (Rp) obtained from the complex non-linear least-squares (CNLS) fitting of the impedance spectra. Although it is generally expected that the more electropositive Ba^{2+} ions would stabilize the higher valence Co^{4+} ions, the arrangement of Ba^{2+} and Gd^{3+} ions in alternating layers is influenced by the significant size difference between them. The smaller Gd^{3+} ions, which tend to adopt a coordination number of less than 12, lead to a reduction in oxygen content in $BaGdCo_2O_{5+\delta}$. This, in turn, increases the number of chemically active sites for the oxygen reduction reaction. Conversely, the smaller size difference between Sr^{2+} and Gd^{3+} ions leads to increased ordering/disordering between the Ba and Gd bilayers, which increases the coordination number and, consequently, the oxygen content in the structure.

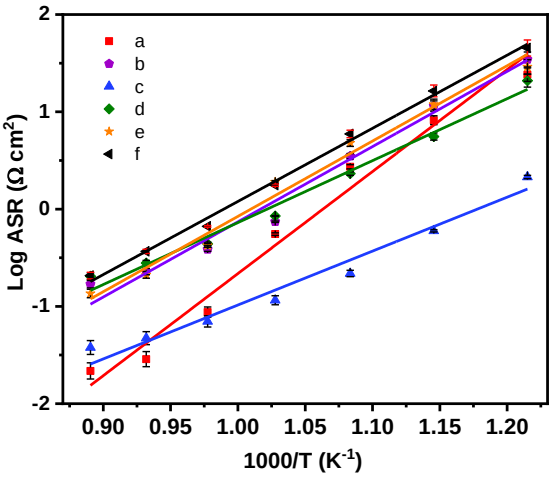

Fig. 12. The Arrhenius plot of a) $Ba_{0.5}Sr_{0.5}CoO_{3-\delta}$, b) $Ba_{0.5}Sr_{0.4}Gd_{0.1}CoO_{3-\delta}$, c) $Ba_{0.5}Sr_{0.3}Gd_{0.2}CoO_{3-\delta}$, d) $BaSr_{0.4}Gd_{0.6}Co_2O_{5+\delta}$, e) $BaSr_{0.2}Gd_{0.8}Co_2O_{5+\delta}$, f) $BaGdCo_2O_{5+\delta}$ cathodes. The error bars correspond to the propagated fitting errors derived from the EIS equivalent circuit analysis

Although the activation energies obtained for all samples are significantly lower than those reported in previous studies [22], the values for $Ba_{05}Sr_{03}Gd_{02}CoO_{3-\delta}$ and $BaSr_{0.4}Gd_{0.6}Co_2O_{5+\delta}$ are particularly low, calculated at 0.46 eV and 0.54 eV, respectively.

Table 2. Summary of activation energies of the BSGC samples on SDC electrolyte in the symmetric cell

Sample	E_a (eV)		
	R_1	R_2	R_p
$Ba_{0.5}Sr_{0.5}CoO_{3-\delta}$	0.81	0.96	0.84
$Ba_{0.5}Sr_{0.4}Gd_{0.1}CoO_{3-\delta}$	0.57	0.68	0.65
$Ba_{0.5}Sr_{0.3}Gd_{0.2}CoO_{3-\delta}$	0.48	0.49	0.46
$BaSr_{0.4}Gd_{0.6}Co_2O_{5+\delta}$	0.53	0.57	0.54
$BaSr_{0.2}Gd_{0.8}Co_2O_{5+\delta}$	0.70	0.64	0.67
$BaGdCo_2O_{5+\delta}$	0.62	0.61	0.64

These results indicate that the oxygen reduction processes in these materials occur more rapidly and exhibit reduced temperature dependence compared to the other compositions. This enhanced performance may be attributed to the superior oxygen kinetics arising from their mixed simple and double perovskite structures, which provide a greater number of chemically active sites and improved triple-phase boundary (TPB) characteristics, thereby facilitating more efficient oxygen reduction reactions within the cathode materials.

Interestingly, although the activation energies corresponding to both non-charge transfer (R_2) and charge transfer (R_1) reactions vary among all samples, an increase in Gd content up to x= 0.6 in the $BaSr_{0.4}Gd_{0.6}Co_2O_{5+\delta}$ sample results in the activation energy of R_1 becoming lower than that of R_2. In contrast, the opposite trend is observed for $BaSr_{0.2}Gd_{0.8}Co_2O_{5+\delta}$ and BGC samples. This observation suggests that Gd substitution significantly influences both non-charge transfer processes—such as gas diffusion and oxygen surface exchange—and charge transfer mechanisms, including oxygen ion diffusion and the overall oxygen reduction reaction. These effects can be directly correlated with the formation of oxygen vacancies and structural modifications induced by phase transitions.

Notably, despite the mixed structural characteristics observed in the two aforementioned samples, the single-phase BGC composition exhibits the lowest activation energy of 0.64 eV. The improvement in oxygen transport properties in this sample can be ascribed to the presence of cation-ordered structures and the anisotropic nature of oxygen diffusion, which differ substantially from those in non-ordered compounds such as BSC. Consequently, these structural features lead to lower activation energies and enhanced oxygen surface exchange and bulk diffusion coefficients [8].

4. CONCLUSIONS

In this study, novel layered perovskite oxides $Ba_{0.5}Sr_{0.5-x}Gd_xCoO_{3-\delta}$ and $BaSr_{1-x}Gd_xCo_2O_{5+\delta}$ were successfully synthesized and systematically investigated as potential cathode materials for intermediate-temperature solid oxide fuel cells (IT-SOFCs). The results revealed a strong correlation between Gd substitution, structural evolution, and electrochemical performance. In situ XRD analysis demonstrated that increasing Gd content induces partial and complete structural transitions at x= 0.2 and x= 0.4, respectively, leading to the formation of mixed simple and double perovskite phases that enhance oxygen kinetics.

Electrical conductivity measurements indicated that conductivity increases with Gd content, maintaining values above 250 S cm^{-1} even at 250°C. Crucially, the $Ba_{0.5}Sr_{0.3}Gd_{0.2}CoO_{3-\delta}$ composition exhibited the highest oxygen reduction activity among all tested samples, delivering a remarkably low area-specific resistance (ASR) of 0.12 Ω cm^2 at the intermediate temperature of 700°C, which further decreased to a minimum value of 0.04 Ω cm^2 at 850°C. This low ASR at 700°C serves as the key figure of merit for intermediate-temperature applications. The superior performance of this composition was attributed to its mixed perovskite structure, which promotes a high density of active sites at the triple-phase boundary (TPB) and improves oxygen surface exchange and diffusion. Furthermore, activation energy analysis revealed that $Ba_{0.5}Sr_{0.3}Gd_{0.2}CoO_{3-\delta}$ and $BaSr_{0.4}Gd_{0.6}Co_2O_{5+\delta}$ exhibited notably low activation energies (0.46 eV and 0.54 eV, respectively), reflecting enhanced oxygen reduction kinetics and reduced temperature dependence. These improvements are closely related to the presence of oxygen vacancies, cation ordering, and anisotropic oxygen diffusion pathways.

Overall, the findings demonstrate that Gd substitution plays a crucial role in tailoring the structural and electrochemical behavior of Ba–Sr–Co-based perovskites. In particular, $Ba_{0.5}Sr_{0.3}Gd_{0.2}CoO_{3-\delta}$ emerges as a highly promising cathode material for IT-SOFC applications due to its excellent structural stability, high electrical conductivity, and superior oxygen reduction activity.

ACKNOWLEDGMENT

The authors acknowledge Shahid Chamran University of Ahvaz for financial support of this work.

REFERENCES

[1] Zhu, B., “Functional ceria-salt-composite materials for advanced ITSOFC applications”, J. Power Sources, 2003, 114(1), 1–9.

[2] Hung, I. M., Wu, J. S., Hsu, Y. W., and Lee, Y. C., “Effect of morphology of $La_{0.8}Sr_{0.2}Co_{0.2}Fe_{0.8}O_{3-\delta}$ cathode on the electrochemical performance of solid oxide fuel cell”, J. Chinese Chem. Soc., 2012,

59(10), 1329–1336.

[3] Tafaroji, S., Farbod, M., Kazeminezhad, I., and Kheirmand, M., "Effect of pre-sintering temperature and ball-milling on the conductivity of $Ba_{0.5}Sr_{0.5}Co_{0.8}Fe_{0.2}O_{3-\delta}$ as a cathode for solid oxide fuel cells prepared by sol-gel thermolysis method", Mater. Res. Express, 2019, 6(9), 095522.

[4] Shirani-Faradonbeh, H. and Paydar, M. H., "Electrical behavior of the Ruddlesden–Popper phase, $(Nd_{0.9}La_{0.1})_2$ $Ni_{0.75}Cu_{0.25}O_4$ (NLNC) and NLNC-x wt% $Sm_{0.2}Ce_{0.8}O_{1.9}$ (SDC) (x= 10, 30 and 50), as intermediate-temperature solid oxide fuel cells cathode", Ceram. Int., 2018, 44(2), 1971–1977.

[5] Zhou, Q., He, T., and Ji, Y., "$SmBaCo_2O_{5+x}$ double-perovskite structure cathode material for intermediate-temperature solid-oxide fuel cells", J. Power Sources, 2008, 185(2), 754–758.

[6] Saha-Dasgupta, T., "Double perovskites with 3d and 4d/5d transition metals: compounds with promises", Mater. Res. Express, 2020, 7(1), 014003.

[7] Gu, H., Yang, G., Hu, Y., Liang, M., Chen, S., Ran, R., Xu, M., Wang, W., Zhou, W., and Shao, Z., "Enhancing the oxygen reduction activity of $PrBaCo_2O_{5+\delta}$ double perovskite cathode by tailoring the calcination temperatures", Int. J. Hydrogen Energy, 2020, 45(48), 25996–26004.

[8] Tarancón, A., Burriel, M., Santiso, J., Skinner, S. J., and Kilner, J. A., "Advances in layered oxide cathodes for intermediate temperature solid oxide fuel cells", J. Mater. Chem., 2010, 20(19), 3799–3813.

[9] Zheng, F. and Pang, S., "Progress in Developing $LnBaCo_2O_{5+\delta}$ as an Oxygen Reduction Catalyst for Solid Oxide Fuel Cells", Catalysts, 2023, 13(9), 1288.

[10] Kim, J. H. and Manthiram, A., "Layered $LnBaCo_2O_{5+\delta}$ perovskite cathodes for solid oxide fuel cells: An overview and perspective", J. Mater. Chem. A, 2015, 3(48), 24195–24210.

[11] Maignan, A., Martin, C., Pelloquin, D., Nguyen, N., and Raveau, B., "Structural and Magnetic Studies of Ordered Oxygen-Deficient Perovskites $LnBaCo_2O_{5+\delta}$, Closely Related to the '112' Structure", J. Solid State Chem., 1999, 142(2), 247–260.

[12] Song, S., Yi, Y., Ran, R., Zhou, W., and Wang, W., "Recent Advances in Barium Cobaltite-Based Perovskite Oxides as Cathodes for Intermediate-Temperature Solid Oxide Fuel", Small | Nanoscience & Nanotechnology Journal, 2024, 20(49), 2406627.

[13] Zhang, R., Xiang, B., Xu, L., Xia, L., and Lu, C., "Density functional theory (DFT) investigation on the structure and photo-catalysis properties of double-perovskite $Gd_{1-x}Ca_xBaCo_2O_{5+\delta}$ ($0\leq x\leq 0.4$)", RSC Adv., 2019, 9(35), 20161–20168.

[14] Wei, B., Lü, Z., Jia, D., Huang, X., Zhang, Y., and Su, W., "Thermal expansion and electrochemical properties of Ni-doped $GdBaCo_2O_{5+\delta}$ double-perovskite type oxides", Int. J. Hydrogen Energy, 2010, 35(8), 3775–3782.

[15] Liu, J., Jin, F., Yang, X., Niu, B., Li, Y., and He, T., "$YBaCo_2O_{5+\delta}$-based double-perovskite cathodes for intermediate-temperature solid oxide fuel cells with simultaneously improved structural stability and thermal expansion properties", Electrochim. Acta, 2019, 297, 344–354.

[16] Wei, B., Lü, Z., Wei, T., Jia, D., Huang, X., Zhang, Y., Miao, J., and Su, W., "Nanosized $Ce_{0.8}Sm_{0.2}O_{1.9}$ infiltrated $GdBaCo_2O_{5+\delta}$ cathodes for intermediate-temperature solid oxide fuel cells", Int. J. Hydrogen Energy, 2011, 36(10), 6151–6159.

[17] Chen, D., Ran, R., and Shao, Z., "Assessment of $PrBaCo_2O_{5+\delta}$+$Sm_{0.2}Ce_{0.8}O_{1.9}$ composites prepared by physical mixing as electrodes of solid oxide fuel cells", J. Power Sources, 2010, 195(21), 7187–7195.

[18] Jun, A., Kim, J., Shin, J., and Kim, G., "Optimization of Sr content in layered $SmBa_{1-x}Sr_xCo_2O_{5+\delta}$ perovskite cathodes for intermediate-temperature solid oxide fuel cells", Int. J. Hydrogen Energy, 2012, 37(23), 18381–18388.

[19] Hu, T., Xu, Y., Xu, K., Zhu, F., and Chen, Y., "Visiting the roles of Sr- or Ca- doping on the oxygen reduction reaction activity and stability of a perovskite cathode for proton conducting solid oxide fuel cells", SusMat, 2023, 3(1), 91–101.

[20] Anjum, U., Vashishtha, S., Agarwal, M., Tiwari, P., Sinha, N., Agrawal, A., Basu, S., and Haider, M. A., "Oxygen anion diffusion in double perovskite $GdBaCo_2O_{5+\delta}$ and

$LnBa_{0.5}Sr_{0.5}Co_{2-x}Fe_xO_{5+\delta}$ (Ln= Gd, Pr, Nd) electrodes", Int. J. Hydrogen Energy, 2016, 41(18), 7631–7640.

[21] Ishizawa, N., Asaka, T., Kudo, T., Fukuda, K., Yasuhara, A., Abe, N., and Arima, T., "Structural Evolution of $GdBaCo_2O_{5+\delta}$ (δ= 7/18) at Elevated Temperatures", Chem. Mater., 2014, 26(22), 6503–6517.

[22] Chang, A., Skinner, S., and Kilner, J., "Electrical properties of $GdBaCo_2O_{5+x}$ for ITSOFC applications", Solid State Ionics, 2006, 177(19–25), 2009–2011.

[23] Tarancon, A., Marrerolpez, D., Penamartinez, J., Ruizmorales, J., and Nunez, P., "Effect of phase transition on high-temperature electrical properties of $GdBaCo_2O_{5+x}$ layered perovskite", Solid State Ionics, 2008, 179(17–18), 611–618.

[24] Wei, B., Lü, Z., Huang, X., Liu, M., Li, N., and Su, W., "Synthesis, electrical and electro-chemical properties of $Ba_{0.5}Sr_{0.5}Zn_{0.2}Fe_{0.8}O_{3-\delta}$ perovskite oxide for IT-SOFC cathode", J. Power Sources, 2007, 176(1), 1–8.

[25] de la Calle, C., Alonso, J. A., Aguadero, A., and Fernández-Díaz, M. T., "Phase trans-formations in $Sr_{0.8}Ba_{0.2}CoO_{2.5}$ brownmillerite: correlation between structure and transport properties", Dalt. Trans., 2009, 21, 4104–1414.

[26] de la Calle, C., Alonso, J. A., and Fernández-Díaz, M. T., "Polymorphism of $Ba_{1-x}Sr_xCoO_{3-\delta}$ ($0\leq x\leq 1$) Perovskites: A Thermal and Structural Study by Neutron Diffraction", Zeitschrift für Naturforsch. B, 2008, 63(6), 647–654.

[27] Parfitt, D., Chroneos, A., Tarancón, A., and Kilner, J. A., "Oxygen ion diffusion in cation ordered/disordered $GdBaCo_2O_{5+\delta}$", J. Mater. Chem., 2011, 21(7), 2183–2186.

[28] Chavez, E., Mueller, M., Mogni, L., and Caneiro, A., "Study of $LnBaCo_2O_{6-\delta}$ (Ln= Pr, Nd, Sm and Gd) double perovskites as new cathode material for IT-SOFC", J. Phys. Conf. Ser., 2009, 167, 0–6.

[29] Lim, C., Jun, A., Jo, H., Ok, K. M., Shin, J., Ju, Y. W., and Kim, G., "Influence of Ca-doping in layered perovskite $PrBaCo_2O_{5+\delta}$ on the phase transition and cathodic performance of a solid oxide fuel cell", J. Mater. Chem. A, 2016, 4(17), 6479–6486.

[30] Kim, J.-H., Prado, F., and Manthiram, A., "Characterization of $GdBa_{1-x}Sr_xCo_2O_{5+\delta}$ ($0\leq x\leq 1.0$) Double Perovskites as Cathodes for Solid Oxide Fuel Cells", J. Electrochem. Soc., 2008, 155(10), B1023.

[31] Gu, C. and Cooper, D. M. F., "Ca^{2+}, Sr^{2+}, and Ba^{2+} Identify Distinct Regulatory Sites on Adenylyl Cyclase (AC) Types VI and VIII and Consolidate the Apposition of Capacitative Cation Entry Channels and Ca2+-sensitive ACs*", J. Biol. Chem., 2000, 275(10), 6980–6986.

[32] Yilmaz, S. and Celen, C., "Synthesis and microstructural characterization of δ-phase bismuth-based electroceramic systems by double-doping regime", Int. J. Appl. Ceram. Technol., 2018, 15(2), 391–398.

[33] Shiiba, H., Nakayama, M., Kasuga, T., Grimes, R. W., and Kilner, J. A., "Calculation of arrangement of oxygen ions and vacancies in double perovskite $GdBaCo_2O_{5+\delta}$ by first-principles DFT with Monte Carlo simulations", Phys. Chem. Chem. Phys., 2013, 15(25), 10494–10499.

[34] Zhang, J., Li, X., Zhang, Z., Xu, X., Chen, Y., Song, Y., Dai, J., Yang, G., Ran, R., Zhou, W., and Shao, Z., "A new highly active and CO_2-stable perovskite-type cathode material for solid oxide fuel cells developed from A- and B-site cation synergy", J. Power Sources, 2020, 457(March), 227995.

[35] Xu, X., Wang, W., Zhou, W., and Shao, Z., "Recent Advances in Novel Nanostructuring Methods of Perovskite Electrocatalysts for Energy-Related Applications", Small Methods, 2018, 2(7), 1–35.

[36] Kim, J. H., Kim, Y., Connor, P. A., Irvine, J. T. S., Bae, J., and Zhou, W., "Structural, thermal and electrochemical properties of layered perovskite $SmBaCo_2O_{5+d}$, a potential cathode material for intermediate-temperature solid oxide fuel cells", J. Power Sources, 2009, 194(2), 704–711.

[37] Yáng, Z., Harvey, A. S., Infortuna, A., Schoonman, J., and Gauckler, L. J., "Electrical conductivity and defect chemistry of $Ba_xSr_{1-x}CoyFe_{1-y}O_{3-\delta}$ perovskites", J. Solid State Electrochem., 2011, 15(2), 277–284.

[38] Baek, K. S., Baek, S. W., Kang, H., Choi, W., Park, J. W., Saxin, S., Lee, S. K., and Kim, J. K., "Electrical conductivity characteristics of Sr substituted layered perovskite cathode ($SmBa_{0.5}Sr_{0.5}Co_2O_{5+d}$) for intermediate temperature-operating solid oxide fuel cell", Ceramics International, 2022, 48(11),

15770-15779.

[39] Zhou, Q., Wang, F., Shen, Y., and He, T., "Performances of $LnBaCo_2O_{5+x}$–$Ce_{0.8}Sm_{0.2}O_{1.9}$ composite cathodes for intermediate-temperature solid oxide fuel cells", J. Power Sources, 2010, 195(8), 2174–2181.

[40] Takahashi, H., Munakata, F., and Yamanaka, M., "Ab initio study of the electronic structures in $LaCoO_3$−$SrCoO_3$ systems", Phys. Rev. B, 1998, 57(24), 15211–15218.

[41] Zeng, P., Chen, Z., Zhou, W., Gu, H., Shao, Z., and Liu, S., "Re-evaluation of $Ba_{0.5}Sr_{0.5}Co_{0.8}Fe_{0.2}O_{3-\delta}$ perovskite as oxygen semi-permeable membrane", J. Memb. Sci., 2007, 291, 148–156.

[42] Celorrio, V., Tiwari, D., and Fermin, D. J., "Composition-Dependent Reactivity of $Ba_{0.5}Sr_{0.5}Co_xFe_{1-x}O_{3-\delta}$ toward the Oxygen Reduction Reaction", J. Phys. Chem. C, 2016, 120(39), 22291–22297.

[43] Kim, J.-H. and Manthiram, A., "$LnBaCo_2O_{5+\delta}$ Oxides as Cathodes for Intermediate-Temperature Solid Oxide Fuel Cells", J. Electrochem. Soc., 2008, 155(4), B385.

[44] Zhou, W., Jin, W., Zhu, Z., and Shao, Z., "Structural, electrical and electrochemical characterizations of $SrNb_{0.1}Co_{0.9}O_{3-\delta}$ as a cathode of solid oxide fuel cells operating below 600 C", Int. J. Hydrogen Energy, 2010, 35(3), 1356–1366.

[45] Zhang, J., Guo, H., Lei, L., Shen, S., Zheng, K., and Han, M., "A critical review of the Butler-Volmer equation for the activation polarization of solid oxide fuel cells", J. Power Sources, 2024, 613, 234871.

[46] Choi, S., Park, S., Kim, J., Lim, T. H., Shin, J., and Kim, G., "Electrochemical properties of an ordered perovskite $LaBaCo_2O_{5+\delta}$-$Ce_{0.9}Gd_{0.1}O_{2-\delta}$ composite cathode with strontium doping for intermediate-temperature solid oxide fuel cells", Electrochem. commun., 2013, 34(3), 5–8.

[47] Park, S., Choi, S., Shin, J., and Kim, G., "A collaborative study of sintering and composite effects for a $PrBa_{0.5}Sr_{0.5}Co_{1.5}Fe_{0.5}O_{5+\delta}$ IT-SOFC cathode", RSC Adv., 2014, 4(4), 1775–1781.

[48] Choi, S., Park, S., Shin, J., and Kim, G., "The effect of calcium doping on the improvement of performance and durability in a layered perovskite cathode for intermediate-temperature solid oxide fuel cells", J. Mater. Chem. A, 2015, 3(11), 6088–6095.

[49] Barbucci, A., Viviani, M., Panizza, M., Delucchi, M., and Cerisola, G., "Analysis of the oxygen reduction process on SOFC composite electrodes", J. Appl. Electrochem., 2005, 35(4), 399–403.

[50] Yin, Y., Liu, B., Yan, D., Li, J., and Jia, L., "Balancing intrinsic properties of cathode materials allows high performance for protonic ceramic fuel cells", SusMat, 2024, 4(6) e240.

[51] Baqué, L., Caneiro, A., Moreno, M. S., and Serquis, A., "High performance nanostructured IT-SOFC cathodes prepared by novel chemical method", Electrochem. commun., 2008, 10(12), 1905–1908.